GLOBAL SIMULATIONS OF THE INTERACTION OF MICROQUASAR JETS WITH A STELLAR WIND IN HIGH-MASS X-RAY BINARIES

Yoon, D.[1] & Heinz, S.[1]
Accepted to ApJ on January 6, 2015

ABSTRACT

Jets powered by high-mass X-ray binaries must traverse the powerful wind of the companion star. We present the first global 3D simulations of jet-wind interaction in high-mass X-ray binaries. We show that the wind momentum flux intercepted by the jet can lead to significant bending of the jet and that jets propagating through a spherical wind will be bent to an asymptotic angle ψ_∞. We derive simple expressions for ψ_∞ as a function of jet power and wind thrust. For known wind parameters, measurements of ψ_∞ can be used to constrain the jet power. In the case of Cygnus X-1, the lack of jet precession as a function of orbital phase observed by the VLBA can be used to put a lower limit on the jet power of $L_{\rm jet} \gtrsim 10^{36} \, {\rm ergs \, s^{-1}}$. We further discuss the case where the initial jet is inclined relative to the binary orbital axis. We also analyze the case of Cygnus X-3 and show that jet bending is likely negligible unless the jet is significantly less powerful or much wider than currently thought. Our numerical investigation is limited to isotropic stellar winds. We discuss the possible effect of wind clumping on jet-wind interaction, which are likely significant, but argue that our limits on jet power for Cygnus X-1 are likely unaffected by clumping unless the global wind mass loss rate is orders of magnitude below the commonly assumed range for Cyg X-1.

Subject headings: x-ray binaries, microquasars, jets

1. INTRODUCTION

X-ray binaries consist of a compact object, such as a neutron star (*e.g.*, Sco X-1, Hjellming et al. 1990) or a black hole (*e.g.* Cygnus X-1, Orosz et al. 2011; Cygnus X-3, Zdziarski et al. 2013), accreting mass from a companion. In certain spectral states, the accretion flow near the compact object generates powerful, collimated jets (Mirabel & Rodríguez 1999; Gallo et al. 2005). These jets appear remarkably similar to the jets produced by supermassive black holes (SMBH) in active galactic nuclei (AGN) in morphology, spectral properties, and energetics (when set in relation to the overall energy released by accretion).

The mostly featureless non-thermal spectra of relativistic jets limit quantitative analysis of jet properties to relatively coarse estimates. However, the propagation of jets and their interaction with the environment offers a very powerful way to study jet properties that complements direct studies of jets themselves. The observations of cavities in galaxy clusters by the *Chandra* X-ray Telescope offer an example of how jet-environment interactions can be used to constrain the properties of large samples of AGN jets (e.g. McNamara & Nulsen 2007, and references therein).

A sub-class in the study of jet-environment interactions involves cases where the accreting black hole launching the jets is moving relative to the surrounding medium. In AGN, when the black hole is moving with considerable speed with respect to the environment, the radio emitting jets are swept backward by ram pressure, generating a bow shock ahead of the moving black hole. AGN jets that show bent morphology are often called "bent doubles" or tailed radio sources (Begelman et al. 1979;

Freeland & Wilcots 2011; Morsony et al. 2013).

It has been suggested that a subset of low mass x-ray binaries (LMXBs) that move through the ISM at high speed due to the kick velocity the LMXB received in the supernova explosion should also exhibit bow shocks and trailing neck structures (Heinz et al. 2008; Wiersema et al. 2009; Yoon et al. 2011), very similar to the case of bent-double AGN sources.

However, an aspect that makes jet propagation in X-ray binaries fundamentally different from AGN jets is the presence of the companion star. The early type companion stars of high mass X-ray Binaries (HMXBs) drive powerful winds in the vicinity of the compact object, which are often the source of accretion in these objects. The wind mass loss rates of the OB-type donor star can be substantial: $\dot{M}_{\rm wind} \sim 10^{-7} - 10^{-5} \, {\rm M_\odot \, yr^{-1}}$. The stellar wind dominates the HMXBs' circum-binary environment compared to any winds launched by the accretion flow. In this work, we study the dynamics and evolution of the jets affected by spherical stellar winds from OB-type donor stars in HMXBs. A subset of HMXB systems consist of a Wolf-Rayet star in orbit with a black hole (*e.g.* Cygnus X-3 Martí et al. 2001; Zdziarski et al. 2013); the mass-loss rate from Wolf-Rayet stars is even higher than that from OB-type stars. Moreover, the Wolf-Rayet star in Cygnus X-3 is tidally locked to the 4.8-h orbital period, resulting in a considerable equatorial enhancement of the mass-loss rate (van Kerkwijk 1993). An investigation of non-spherical and highly-flattened winds is beyond the scope of this study. While we briefly discuss the case of Cygnus X-3 under the assumption of a spherical wind, we plan to discuss the effects of non-spherical winds in a future paper.

HMXB winds are not simple. For example, they are likely clumpy (Owocki et al. 1988; Oskinova et al. 2012), like winds generated by other high-mass stars.

yoon@astro.wisc.edu
[1] Department of Astronomy, University of Wisconsin-Madison, Madison, WI, USA

The interaction of a microquasar jet with clumpy wind medium has been studied in 3D simulations by Perucho & Bosch-Ramon (2012), which we will refer to as P12 hereafter, who show that clumping can significantly increase jet disruption. Moreover, even on average, they are not spherically symmetric due to the gravitational focusing by the compact object and Coriolis and centrifugal effects due to orbital motion (Friend & Castor 1982; Miller et al. 2005; Hadrava & Čechura 2012). In addition, the wind can be ionized by X-rays from the accretion flow, reducing or eliminating line driving and stalling the wind (Gies et al. 2008). If the X-ray flux is high enough to excite the outer layer of the star, a thermally driven wind may replace the quenched radiatively driven wind. At the current time, it is not clear whether the illuminated side of the wind would suffer from the same line-driving instability that generates clumps in regular massive star winds.

In this pilot paper, we will neglect some of the more poorly understood complications likely present in binary winds and instead treat the wind as a radiatively driven wind that is isotropic at the surface of the companion (following, e.g. Castor et al. 1975). This will allow us to isolate the fundamental differences in jet propagation in the presence of a wind compared to jets propagating into uniform medium. We will discuss the effects of some of the likely complications in §4.7. The likely most important caveat is the potential clumpiness of the wind; in that sense, the global simulations presented below should be considered a complementary approach to the detailed 3D jet-clump simulations presented in P12.

In §2, we present the numerical setup and the code used in our parameter study of jet-wind interaction. In §3 we discuss the results of the simulations. In §4, we compare the numerical results with analytic expressions derived for the limiting case of small deflection angles and apply our model to the HMXBs Cygnus X-1 and Cygnus X-3. In §5 we summarize our results.

2. TECHNICAL DESCRIPTION

2.1. *The FLASH Code*

Simulations were performed with the FLASH 3.3 hydrodynamics code (Fryxell et al. 2000), which is a Message Passing Interface(MPI)-parallelized, modular, block-structured adaptive mesh refinement code. We employ the non-relativistic unsplit mesh solver, which solves the Riemann problem using an unsplit staggered mesh scheme on a three dimensional Cartesian grid (Lee & Deane 2009).

2.2. *The Wind and Jet Nozzles*

Both the jet and the wind injection are modeled as inflow-boundary conditions on an interior portion of the grid (we will refer to the regions excluded from the hydrodynamic integration and instead treated as an interior boundary as "nozzles" following Heinz et al. 2006).

The jet nozzle has a cylindrical shape with inflow boundary conditions at the surface, injecting a bipolar outflow with a prescribed energy, mass, and momentum flux to match the parameters we choose for the jet. For reasons of numerical stability, we inject a slow lateral outflow from the side walls of the cylinder with negligible mass and energy flux in order to avoid complete evacuation of zones adjacent to the nozzle due to the large velocity divergence along the jet axis.

The stellar wind nozzle is modeled as a spherical boundary with inflow boundary conditions matching the desired wind parameters. We evolve the simulation with only the stellar wind present for one full orbital period to establish a stable, self-consistent wind profile before switching on the jet nozzle.

The equation of state is assumed to be adiabatic, tracking two separate phases of the fluid (each represented by a separate passive tracer fluid to distinguish wind and jet fluids during the computation and in post-processing). The wind gas is assumed to be a monatomic ideal gas with an adiabatic index of $\gamma = 5/3$. The internal composition of jets is currently unknown, however, it is reasonable to assume that they are strongly magnetized and that a sizeable fraction of their internal energy is carried by relativistic electrons, given the observed synchrotron radiation. We investigate jets composed of fluids both with relativistic equation of state with $\gamma = 4/3$ and with a cold-gas equation of state with $\gamma = 5/3$ and present results in terms of an unspecified value of γ wherever possible.

Most simulations were performed using $\gamma = 4/3$, representing the equation of state for a gas with relativistic internal pressure, either from a fully tangled magnetic field (Heinz & Begelman 2000) or a relativistic component of the gas; since our simulations are sub-relativistic, a relativistic equation of state implies that the inertial density is dominated by cold particles (e.g., protons). A non-relativistic equation of state represents a jet with internal pressure dominated by non-relativistic thermal plasma. As we will show, our results are only moderately sensitive to the actual value of γ.

The gravitational fields of the black hole and the companion are modeled as point source potentials.

To allow for direct comparison with the analytic formulae we derive in §4.2, most of the simulations presented in this paper do not include wind driving by radiation pressure. Instead, we assumed an asymptotic wind at the injection at the stellar surface, *i.e.*, a wind with terminal velocity v_∞ and at fixed mass flux of $\dot{M}_{\text{wind}} \sim 10^{-5} \, M_\odot \, \text{yr}^{-1}$, which is typical for OB stars (Puls et al. 2008).

Wind driving was incorporated in a sub-set of the simulations presented in this paper to test the sensitivity of our results against the assumption of an asymptotic radial wind. (See §4.3). For the radiatively driven wind, the initial velocity field follows the so-called β-law

$$v(r) = v_\infty (1 - r_0/r)^\beta, \qquad (1)$$

where $v_\infty = 2,500 \, \text{km s}^{-1}$ is the wind terminal speed [chosen to match the wind parameters of typical OB-type stars (Puls et al. 2008)] and $r_0 = R_* x$, where R_* is the radius of the star and x is applied to avoid zero velocity and infinite density on the surface of the star. We set the stellar radius $R_* = 1.4 \times 10^{12} \, \text{cm}$. The value of x can be expressed as $x = \left[1 - (v_*/v_\infty)^{1/\beta} \right] = 0.99$, where the wind surface velocity, v_*, is of the order of 10^6cm s^{-1}, which is the sound speed with $T_{\text{eff}} \approx 30,000 \, K$. However, due to the steep variation of density and pressure around the surface, there is a limit in performing a numerical

calculation with such a high value of x. Alternatively, we set the value of $x = 0.95$, which was chosen to be high enough to maintain the initial wind profile from a typical OB-type star by iterative 1D simulations. The mass flux of the wind was fixed at the surface of the star (where density and velocity of the injected wind determine $\dot{M}$ uniquely) and line driving was modeled using the Sobolev approximation (Castor 1974), such that the total line acceleration results in $g_{\rm rad} \propto \left(\frac{1}{\rho}\frac{dv_r}{dr}\right)^{\alpha_{\rm CAK}}$, where $\alpha_{\rm CAK}$ is the parameter of the CAK model (Castor et al. 1975), typically depending on the effective temperature of the star. We choose a value of $\alpha_{\rm CAK} = 0.64$ in our model corresponding to a typical OB-type star.

Our simulations are adiabatic and scale-free. In physical units chosen to approximately match the wind and binary properties of Cygnus X-1 and allow simulations to be completed within the available computational resources, the jet velocity was set to be $v_{\rm jet} = 3 \times 10^9\,{\rm cm\,s^{-1}}$, with an initial internal Mach number of $\mathcal{M}_{\rm jet,0} = 30$ at the base of the jet (the "nozzle"). To explore the dependence on Mach number, we ran a simulation at $\mathcal{M}_{\rm jet,0} = 10$ and otherwise identical parameters compared to our fiducial run with a jet power of $L_{\rm jet} = 10^{36}\,{\rm ergs\,s^{-1}}$. Note that the Mach number $\mathcal{M}_{\rm jet}$ varies along the jet given the adiabatic behavior of the fluid.

In order to resolve the hydrodynamics at the injection scale with at least 10 cells across the nozzle, we forced the jet nozzle to be at maximum refinement, resulting in an effective resolution of $4.7 \times 10^9\,{\rm cm} = 1.6 \times 10^{-3}\,a$, compared to an orbital separation of $a \approx 3 \times 10^{12}\,{\rm cm}$ for Cygnus X-1 (Gies & Bolton 1982). The radius of the jet nozzle is about $2.5 \times 10^{10}\,{\rm cm}$ and the full box size of the simulation is about $4 \times 10^{13}\,{\rm cm}$, centered on the center of mass of the binary.

We varied the jet power to span the range $L_{\rm jet} \approx 10^{35},\ 10^{36},\ 10^{37}\,{\rm ergs\,s^{-1}}$, comparable to the range of uncertainty in the jet power of Cygnus X-1, $9 \times 10^{35} - 10^{37}\,{\rm ergs\,s^{-1}}$ (Gallo et al. 2005; Russell et al. 2007).

For the bulk of our simulations, the jet was injected in a direction perpendicular to the orbital plane, *i.e.*, along the z-axis of our grid. We also investigated off-axis jets with angles of $30°$, $60°$, $75°$ relative to the orbital axis of the system, inclined towards the binary companion (inclination angles perpendicular to the orbital separation vector would not result in any change in the simulation, given that simulations only cover a small fraction of the binary period once the jet is switched on). The detailed model parameters of our different runs are described in table 1.

Note also that in cases where the jet is oriented perpendicular to the binary separation vector $\vec{a}$, the simulations have mirror-symmetry about $\vec{a}$; in these cases, in order to reduce the need for computational resources, we only simulate the upper hemisphere at full resolution, but include both hemispheres to avoid spurious boundary effects near the orbital plane. Results in those cases are quoted for the high-resolution half of the simulation.

2.3. Orbital Motion

The binary parameters were set loosely approximate the parameters for of Cygnus X-1. For simplicity, we set the mass of the black hole and the star to be 10 and 20 $M_\odot$, respectively, and the separation between them is set to be $3 \times 10^{12}\,{\rm cm}$, which gives an orbital period of 5.8 days for Cygnus X-1, compared to the observed value of 5.6 days (Brocksopp et al. 1999; Pooley et al. 1999)

As we show below, the jet propagation time across one binary separation (1.7 minutes) and the time required for a quasi-stationary bent jet solution to be established (approximately 10 hours) is much shorter than the orbital time. For numerical simplicity and to allow direct comparison with the analytic formulae presented in §4.2, we neglected orbital rotation in most of our simulations, keeping the two nozzles stationary in our cartesian grid. As a first order approximation, this is justified because the orbital velocity is only of order 20% of the wind velocity, and thus orbital effects on the wind ram pressure introduce corrections of the order of only 5%.

In order to verify that the effects of orbital motion on the gross dynamics of jet propagation are small, we ran a sub-set of the simulations including orbital rotation, presented in §4.2. In this case, the nozzles (star and jet) move along their orbital trajectories in the x-y plane (*i.e.*, we simulated the orbit in a fixed, non-rotating frame, which eliminates the need to introduce terms for Coriolis and centrifugal forces into the solver). The coordinate origin was set to be at the center of mass.

In the rotating case, we assumed that the star is co-rotating with the orbit, such that the outflow velocity at the stellar surface is given by

$$\vec{v}_{\rm wind,rot}(\vec{x}) = \vec{\omega} \times \vec{x} + \vec{v}_{\rm wind,*}\left(\vec{x} - \vec{R_*}\right), \qquad (2)$$

where $\vec{\omega}$ is the orbital angular velocity, $\vec{v}_{\rm wind,*}$ the wind velocity at the stellar surface calculated from eq. (1), and $\vec{R_*}$ the position of the star.

We ran the simulations for one orbital period before switching on the jet in order to allow the flow to establish a converged velocity and density profile. After the jet launches, the simulations were carried out for several hours in real time units, long enough to establish the bow shock and the jet in a quasi-steady state (see §2.4).

Finally, we performed a comparison simulation of a jet propagating into a uniform wind with parameters matching those of our fiducial run at the position of the compact object (referred to below as UniWind_E36).

2.4. Measurement of the Jet Thickness and Propagation Direction

A key variable determining the strength of the jet-wind interaction is the thickness h of the jet as seen by the wind (*i.e.*, the size of the jet perpendicular to both jet and wind velocities). We measured h as follows.

In post-processing, we identified matter inside a computational cell as jet material if the value of $\zeta \equiv (v_z/v_{\rm jet})\,J$ exceeded a fixed threshold, where $(v_z/v_{\rm jet})$ is the flow velocity normalized by the initial jet speed, which is $3 \times 10^9\,{\rm cm\,s^{-1}}$ in our standard parametrization, and J is the fractional density of jet tracer fluid injected at the nozzle. We found that a choice of $\zeta = 0.1$ successfully identified the jet material in all cases (see Figure 7). The thickness of the jet was measured in the direction perpendicular to the separation vector and the jet axis, since it is the dimension of the jet in that direction that

Table 1
Model Parameters

Model	$L_{\rm jet}$ (ergs s^{-1})	$\mathcal{M}_{\rm jet,0}$	inclination (degree)	h_1[b] (cm s^{-1})
SphWind_E35	10^{35}	30	0[a]	3×10^{10}
SphWind_E36	10^{36}	30	0	8×10^{10}
SphWind_E36_M10	10^{36}	10	0	1×10^{11}
SphWind_E36_rot	10^{36}	30	0	8×10^{10}
SphWind_E36_acc	10^{36}	30	0	8×10^{10}
SphWind_E36_30deg	10^{36}	30	30	8×10^{10}
SphWind_E36_60deg	10^{36}	30	60	8×10^{10}
SphWind_E36_75deg	10^{36}	30	75	8×10^{10}
SphWind_E37	10^{37}	30	0	1.5×10^{11}
SphWind_E37_gam166	10^{37}	30	0	1.5×10^{11}
UniWind_E36	10^{36}	30	0	8×10^{10}

[a] 0° indicates that the direction of the jet is perpendicular to the line between the star and the Black hole.
[b] The jet thickness at the re-collimation shock, h_1, is measured naively by checking the variation of the jet thickness along the jet from simulation results.

determines the amount of wind momentum flux intercepted by the jet.

When the jet first turns on, it propagates in its initial direction, following the standard evolution of jet propagation until the expansion of the cocoon becomes slower than the wind velocity. As the head of the jet propagates, the accumulated perpendicular momentum flux begins to bend it away from its initial propagation direction. We then traced the propagation direction of the jet fluid to determine the jet trajectory and bending angle.

3. RESULTS

3.1. *Jet Bending in Spherical Winds*

Our simulations confirm the general expectation that a powerful wind from a companion star can affect the propagation of the jet, and that the ultimate trajectory of the jet depends on the relative momentum flux in the wind and the jet, as well as the geometry of the system.

We briefly describe the morphology of the jet-wind interaction and compare it to simulations of jet bending observed in the interaction of a jet with a uniform medium (Yoon et al. 2011). Figure 1 shows snapshots of our fiducial run at a jet power of $L_{\rm jet} = 10^{36}\,{\rm ergs\,s^{-1}}$.

Upon injection into the grid, the jet fluid is generally over-pressured compared to the external pressure and the ram pressure of the stellar wind (the pressure is fixed by our choice of the jet power, the jet velocity, the Mach number, and the cross sectional area of the jet nozzle).

We chose this setup to allow the jet to establish a self-consistent, stable structure by letting the jet reach pressure equilibrium with the bow shock. During this phase, the jet does not experience any bending, given that it is strongly over-pressured with respect to the ram pressure in the stellar wind. We show a typical setup in Figure 1, which displays a density slice through the simulation. Generally, the lack of external confinement leads to free lateral expansion of the jet with a half-opening angle of order $\alpha_0 \sim 1/\mathcal{M}_{\rm jet,0}$. The wind is gravitationally focused by the black hole in the down stream region, generating the density enhancement along the equatorial plane visible to the left of the black hole in Figure 1. Here and in the following, we place the x-axis along the orbital separation vector at t=0 and the z-axis along the orbital angular momentum vector.

The free expansion of the jet proceeds until its pressure reaches the pressure behind the bow shock of the wind, at which point the jet goes through a re-collimation shock and reaches a stable equilibrium thickness h_1. Thus, h_1 is not directly set as a simulation parameter, but instead determined by the initial Mach number of the jet.

However, since neither the re-collimation region nor the initial Mach number of the jet are observable, we will carry out most of the analysis in this paper using the jet thickness h beyond the re-collimation shock, relating it where possible to observables like the large scale opening angle of the jet $\alpha_{\rm obs}$. We will describe the details of the re-collimation region, which is very close to the black hole compared to the size of the simulation box, in §3.2.

The approaching stellar wind material goes through a stationary bow shock as it is forced to propagate around the jet. Beyond the re-collimation shock, the transverse pressure gradient imparted on the jet by the lateral momentum flux of the stellar wind then gradually bends the jet fluid away from the companion star, while the jet thickness h is set by lateral pressure balance with the wind bow shock pressure.

The effects of the radially declining wind density and the changing velocity of the wind as a function of distance along the jet imprint a qualitatively different asymptotic behavior of the jet compared to interaction with a uniform medium. Because the density declines roughly as r^{-2}, where r is the distance from the center of the star, the effect of bending declines with distance, and most of the bending occurs within about a binary orbital separation from the jet nozzle.

More importantly, jet bending is caused only by transverse momentum flux, which depends on the angle $\vartheta = \sin^{-1}\left(\left|\hat{\vec{v}}_{\rm jet} \times \hat{\vec{v}}_{\rm wind}\right|\right)$ between the local jet velocity and wind velocity through $\sin^2(\vartheta)$. Because ϑ decreases with increasing r, the amount of transverse momentum flux also decreases with r. Asymptotically, any initially large ϑ will tend to zero (even in the absence of any jet bending) and the amount of lateral momentum flux across the jet decreases strongly with distance. At infinity, jet and wind travel parallel to each other at some asymptotic angle ψ_∞ relative to the initial jet direction. In contrast, in a uniform wind, ϑ does not decrease with distance from the nozzle, and both jets must eventually be bent such that the jet plasma asymptotically flows parallel to the

wind direction.

We ran simulations with jet powers of $L_{\rm jet} = 10^{35}, 10^{36}, 10^{37}\,{\rm ergs\,s^{-1}}$, and the results are shown in Figure 2. The dashed lines indicate the converged asymptotic lines towards which the jet is bent by the wind, showing that the ψ_∞ is a strong function of jet power. In the case of $L_{\rm jet} = 10^{35}\,{\rm ergs\,s^{-1}}$, the ram pressure by the stellar wind is sufficiently strong to bend the jet by almost 90°, similar to the case of the UniWind_E36 uniform wind model. On the other hand, for the highest jet power case in our simulation, $L_{\rm jet} = 10^{37}\,{\rm ergs\,s^{-1}}$, the bending angle is small. We will discuss the relationship between the jet kinetic power and the inclination angle in §4.2.

We generally find that the jet is bent towards its asymptotic bending angle within a time scale of $\tau_{\rm bend} \sim 0.05\,\tau_{\rm orbit}$, where $\tau_{\rm orbit}$ is the orbital period; this is roughly the time for the geometry of the inner jet to reach a steady state. We measured the propagation direction and asymptotic bending angle of the jet after it settled into its steady state. Note that the short bending time scale $\tau_{\rm bend} << \tau_{\rm orbit}$ implies that the jet reacts instantaneously to changes in binary orbit, which further implies that the jets must be precessing on the orbital period of the system if bent by jet-wind interaction.

Figure 3 explores the dependence of our simulations on the initial internal Mach number of the jets, with $\mathcal{M}_{\rm jet,0}$ set to one third of our fiducial value. With otherwise identical parameters, a smaller Mach number implies larger thermal energy relative to the total energy of jet. The increased thermal pressure leads to a larger initial opening angle of the jet, which in turn results in an increase in transverse momentum transfer and jet bending. The increased surface area and decreased Mach number also increase the incidence of Kelvin-Helmholtz instability and earlier onset of jet disruption.

3.2. The Re-collimation Shock

In order to investigate the physics of jet re-collimation by the wind, we carried out a set of test simulations with significantly increased resolution, restricted to a shorter duration. We performed the tests with two jet Mach numbers, $\mathcal{M}_{\rm jet,0} = 10, 30$. Snapshots of the re-collimation region are shown in Figure 4. We measured the jet thickness along the y-axis (y-z slice) for the analysis below because the effective cross section of the wind momentum flux captured by the jet depends only on the width of the jet in y-direction. Jet bending is facilitated by the pressure gradient in the x-z plane, where only the leading edge of the jet is subject to the increased pressure behind the bow shock.

In our simulations, the jet is initially freely expanding. Acceleration of the lateral expansion will become inefficient once the lateral motion itself becomes supersonic. This sets the characteristic semi-opening angle α_0 of such a supersonic "fan" simply as

$$\alpha_0 \sim \frac{1}{\mathcal{M}_{\rm jet,0}} = \frac{c_{\rm s,0}}{v_{\rm jet}} = \sqrt{\frac{\gamma P_0}{\rho_0}}\frac{1}{v_{\rm jet}}. \quad (3)$$

In Figure 5 we plot the measured jet thickness h as a function of height z. As expected, the jet with the initially higher Mach number has a narrower opening angle.

From the numerical experiment, the initial half-opening angle α_0 of the jet is roughly

$$\alpha_0 \sim \frac{3}{\mathcal{M}_{\rm jet,0}} \quad (4)$$

slightly larger than the simplistic estimate $\alpha_0 \sim 1/\mathcal{M}_{\rm jet,0}$.

Once the conical expansion has been established, the lateral ram pressure $P_{\rm jet,ram,\perp}$ of the jet

$$P_{\rm jet,ram,\perp} = \rho_{\rm jet} \sin^2 \alpha_0\, v_{\rm jet}^2 = \rho_0 \left(\frac{z_0}{z}\right)^2 \sin^2 \alpha_0\, v_{\rm jet}^2 \quad (5)$$

is always larger than the internal pressure (since the lateral expansion is supersonic).

In terms of the kinetic jet power

$$L_{\rm jet,kin} = \pi \rho_{\rm jet} v_{\rm jet}^3 h^2/4 = \pi \rho_{\rm jet} v_{\rm jet}^3 z^2 \sin^2 \alpha_0 \quad (6)$$

the lateral ram pressure is

$$P_{\rm jet,ram,\perp} = \frac{L_{\rm jet,kin}}{\pi z^2 v_{\rm jet}} \quad (7)$$

independent of $\sin \alpha_0$ and $\mathcal{M}_{\rm jet,0}$.

Lateral expansion will proceed until $P_{\rm jet,ram,\perp}$ drops below the pressure in the wind bow shock that forms around the jet, $P_{\rm wind,ram}$. At this point, a re-collimation shock must form in the jet and bring the internal pressure of the jet into equilibrium with the bow shock. We will denote the location of the re-collimation shock along the jet as z_1. For parameters considered in this paper, z_1 is always much smaller than the binary separation a, so we will assume that ram pressure of the wind is constant for the discussion of z_1 and h_1, so the wind ram pressure is given by its value in the equatorial plane at the location of the black hole.

In terms of the mass loss rate of the wind[2], $\dot{\rm M}_{\rm wind} = 4\pi r^2 v_{\rm wind}\rho_{\rm wind} = 4\pi a^2 v_{\rm wind}\rho_{\rm wind,0}$, the wind ram pressure at the jet nozzle is then

$$P_{\rm wind,ram,0} = \rho_{\rm wind,0} v_{\rm wind}^2 = \frac{\dot{\rm M}_{\rm wind} v_{\rm wind}}{4\pi a^2} \quad (8)$$

where, $\rho_{\rm wind,0}$ is the wind density at the footpoint of the jet and $v_{\rm wind}$ is the velocity of the stellar wind, assumed to be constant.

The location of the re-collimation shock z_1 is given by equating $P_{\rm jet,ram,\perp} = P_{\rm wind,ram,0}$:

$$z_1 = a\sqrt{\frac{4\,L_{\rm jet}}{\dot{\rm M}_{\rm wind} v_{\rm wind} v_{\rm jet}}} \quad (9)$$

again independent of $\mathcal{M}_{\rm jet,0}$ and α_0.

This simple picture is qualitatively confirmed by the high-resolution simulations of the re-collimation shock: Figure 5 shows the re-collimation shock at $z \approx 7 \times 10^{11}$ cm regardless of the jet Mach number, consistent within an error range of 20% with the analytic solution $z_1 \approx 9 \times 10^{11}$ cm from eq. (9) for the simulation parameters ($L_{\rm jet} = 10^{37}{\rm ergs\,s^{-1}}$, $\dot{\rm M} = 10^{-5}{\rm M_\odot\,yr^{-1}}$, $v_{\rm wind} = 2.5 \times 10^8$ cm, $v_{\rm jet} = 0.1\,c$, $a = 3 \times 10^{12}$cm).

---

[2] Given typical properties of OB-type stars, the mass loss rate is of order $\dot{\rm M}_{\rm OB} \sim 10^{-7} \sim 10^{-5}\,{\rm M_\odot\,yr^{-1}}$ with a terminal velocity of $v_{\rm wind} \approx 2000 - 3000\,{\rm km\,s^{-1}}$ (Castor et al. 1975; Puls et al. 2008).
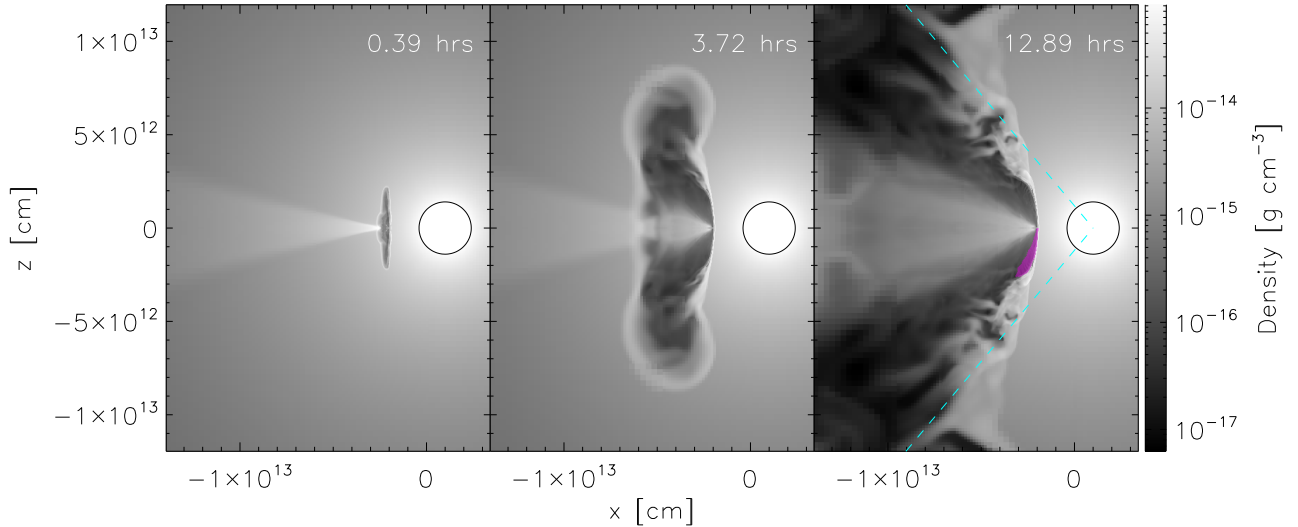
Figure 1. Time sequence of density maps for our fiducial simulation SphWind_E36. The black circle indicates the surface of the companion star. The enhanced density in the down stream of equatorial plane to the left of the black hole is due to the gravitationally focused wind. The bow shock structure along the jet reaches steady state approximately in 12 hours after it launches. The magenta area in the right-most image indicates the jet materials (marked only in the lower half of the image), identified by a certain threshold (see §4.1). The cyan dashed lines in the right-most panel indicate asymptotic lines along which the jets converge, showing that the jet is bent by approximately 30° from the initial direction. In the down-stream region, the bow-shocked wind passes around the jet and re-collimates in an expansion fan and a (weak) re-collimation shock, as expected for super-sonic flow around an object, leaving the post-shock region filled with wind gas, visible in the right-most two panels.
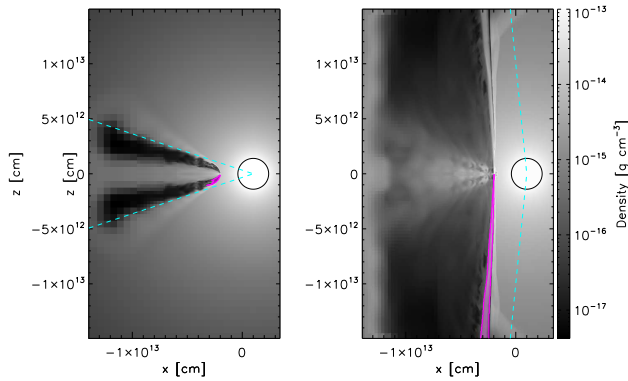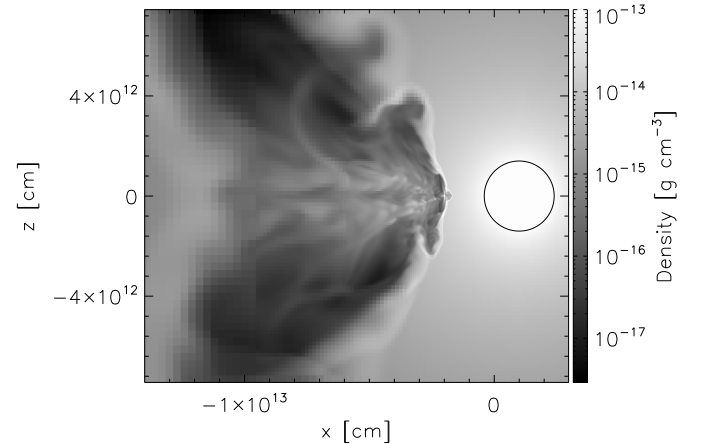

Figure 2. Density maps for the case of SphWind_E35 (left panel) and SphWind_E37 (right panel) after the steady state bow shock structure has been established. While the jet for SphWind_E35 is disrupted within a short distance from its injection, the jet for Sph-Wind_37 is steadily maintained (marked in magenta color). The cyan dashed lines indicate that the jet bending angles are 65° and 8° for SphWind_E35 and SphWind_E37, respectively. The vertical black thin trajectory in right panel is the low density area generated by the shear layer between the jet and the bow shock.

Figure 3. Density map in the case of lower Mach number, $\mathcal{M}_{jet,0}$ = 10 (SphWind_E36_M10).

At the re-collimation shock, the jet will have a thickness h_1 and will be in pressure equilibrium. Beyond z_1, the jet will thus adjust its thickness h to maintain pressure equilibrium with the wind. We will discuss the propagation of the jet in this phase, and the interaction with the wind that occurs beyond z_1, in the next section.

4. DISCUSSION

As described above, the development of an asymptotic bending angle ψ_∞ is expected from simple considerations of the geometry of the interaction between jet and wind.

A full analytic description of the detailed dynamical evolution of the jet (including the onset of dynamical instabilities such as Kelvin-Helmholtz instability) is be-

yond the scope of this paper. Therefore, for the following analysis, we make the assumption that the bending angle ψ of the jet is small (implying relatively weak interaction).

Because non-linear effects (like dynamical instabilities) tend to increase the cross section of the jet, they will tend to increase the bending angle due to the large net transverse momentum intercepted by the jet. In that sense, the relations derived below will be lower limits on the actual bending angle. This is borne out by our simulations (See Figure 9 below).

We will further assume that the wind is asymptotic, *i.e.*, has reached constant velocity before interacting with the jet and thus follows a simple r^{-2} density profile. We will also neglect effects of orbital motion in the analytic approximations below (justified by the fact that they can be expected to be about an order of magnitude smaller than the dominant effects, as argued above).
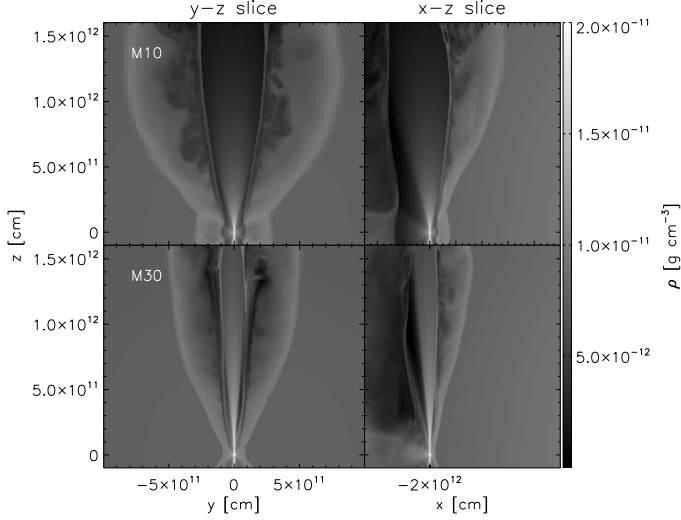
Figure 4. Density map for re-collimating jets in $\mathcal{M}_{\mathrm{jet},0} = 10$ (upper panels), and $\mathcal{M}_{\mathrm{jet},0} = 30$ (lower panels). The jet is re-collimated in the y-z plane while bending occurs in the x-z plane.

4.1. The Evolution of the Jet Thickness Beyond the Re-Collimation Shock

We will assume that the jet is in pressure equilibrium with the ram pressure of the wind,

$$
\begin{aligned}
P_{\mathrm{jet,ram},\perp} &= \rho_{\mathrm{wind}}(\theta)\left(v_{\mathrm{wind}}\cos^2\theta\right)^2 \\
&= \rho_{\mathrm{wind},0}v_{\mathrm{wind}}^2\cos^4\theta \\
&= \rho_{\mathrm{wind},0}v_{\mathrm{wind}}^2\left(\frac{a^2}{a^2+z^2}\right)^2
\end{aligned}
\tag{10}
$$

where we have used $\cos\theta = a/\sqrt{a^2+z^2}$, where θ is the angle between the orbital separation vector $\vec{a}$ connecting the star and the black hole, and the vector $\vec{r}$ from the star to a given position along the jet. The jet has an initial jet thickness h_1, as discussed above, which we take as a parameter in the following.

The geometry of the jet and the re-collimation shock and the definitions of the relevant angles and coordinate axes are sketched in Figure 6.

Beyond the re-collimation shock, the jet thickness h follows from pressure equilibrium between the jet and the bow shock:

$$
\begin{aligned}
P_{\mathrm{jet,ram},\perp} &= \rho_{\mathrm{wind},0}v_{\mathrm{wind}}^2\left(\frac{a^2}{a^2+z^2}\right)^2 \\
&= P_{\mathrm{jet}} = P_{\mathrm{eq},1}\left[\frac{h(z)}{h_1}\right]^{-2\gamma}
\end{aligned}
\tag{11}
$$

where $P_{eq,1}$ and h_1 are the pressure and the jet thickness at the re-collimation shock. This sets the jet thickness h:

$$
h\left(z\right) = h_1\left(\frac{a^2}{a^2+z^2}\right)^{-1/\gamma}
\tag{12}
$$

Figure 7 shows the measured jet thickness h as a function of z for simulation SphWind_E37, compared to the value calculated from eq. (12), for different choices of the jet threshold (see §2.4). The figures show good agreement between the model and the simulation.

Generally, h_1 will not be measurable. However, we can us eq. (12) to relate a measured jet thickness (or an upper limit) at large z to the jet thickness at any other z, given values for γ and a.

Stirling et al. (2001) reported that the VLBA jet of Cygnus X-1 has a semi-opening angle of $\alpha_{\mathrm{VLBA}} = h/2\,z_{\mathrm{VLBA}} \lesssim 2°$, where z_{VLBA} is the scale length of the extended jet on which the opening angle is measured; the orbital separation and the length of the jet are 0.1 mas and 15 mas, respectively. By using eq. (12) with $\gamma = 4/3$, the jet thickness at the re-collimation shock can be estimated as $h_1 \lesssim 5.7 \times 10^{-3}\,a$. For a value of $\gamma = 5/3$, we find a value of $h_1 \lesssim 1.3 \times 10^{-2}\,a$. We will further discuss the constraints on the initial half-opening angle in the case of the Cygnus X-1 jet in §4.4.

4.2. Jet Bending and the Asymptotic Bending Angle

With an expression for the jet thickness h from eq. (12), we can now discuss the amount of bending experienced by the jet. Technically, jet bending occurs because a transverse pressure gradient exists behind the bow shock that the wind drives around the jet, such that the external pressure at the leading edge is $P_1 \sim P_{\mathrm{bow}}$ and the pressure on the trailing edge of the jet is $P_2 \ll P_1$. Thus, a transverse pressure gradient exists inside the jet as well, acting to accelerate/bend the jet fluid away from the star.

In deriving an estimate for ψ_∞, we will make the simplifying assumption that the bending angle is small, *i.e.*, that the accumulated transverse momentum flux is small compared to the lateral momentum flux. The reason for this assumption is that the jet will be dynamically disrupted if the bending angle is large, as the jet-boundary interaction must be significant in this case. Our simulations bear out the validity of this assumption at least in the hydrodynamic case studied here. Similarly, we neglect the momentum transfer from the wind to the jet in the longitudinal direction, which would lead to acceleration or deceleration by a small amount.

Based on the properties of observed astrophysical jets (the presence of shocks, the inferred large kinetic power compared to the minimum internal energy based on the observed synchrotron intensity), we further assume the jet to be supersonic (large internal Mach number) and ballistic (no further acceleration beyond the nozzle). This reflects the setup of our simulations.

Under the assumption of constant longitudinal jet velocity and $\mathcal{M}_{\mathrm{jet},0}^2 \gg 1$, the longitudinal jet momentum per unit jet length is conserved and given by

$$
\begin{aligned}
\Phi_{m,\mathrm{jet}} &= \int dA_\perp \rho_{\mathrm{jet}}v_{\mathrm{jet}} \\
&= \pi\,r_{\mathrm{jet},0}^2\,\rho_{\mathrm{jet},0}\,v_{\mathrm{jet}} \\
&= \frac{L_{\mathrm{jet,kin}}}{v_{\mathrm{jet}}^2},
\end{aligned}
\tag{13}
$$

where $dA_\perp$ is the area element perpendicular to the initial jet direction, $r_{\mathrm{jet},0}$ and $\rho_{\mathrm{jet},0}$ are the radius and the density of the jet at the nozzle.

The transverse momentum per unit jet length accumu-
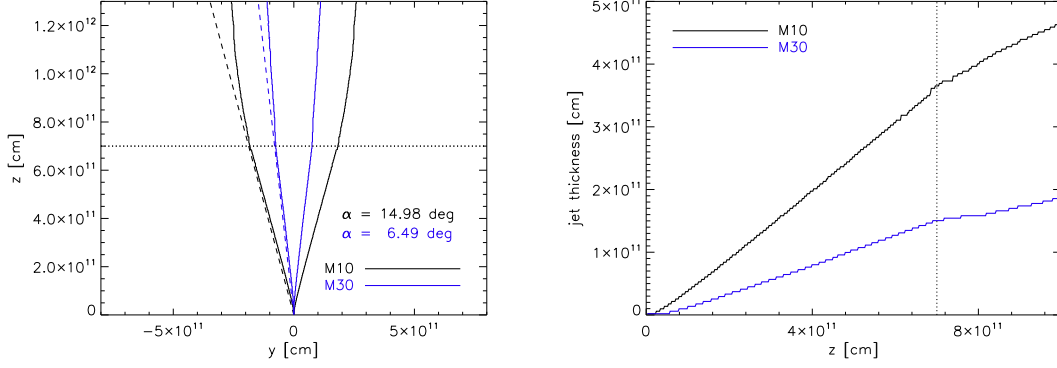
Figure 5. Left panel: Identified jets from simulation for the case of $\mathcal{M}_{\text{jet},0} = 10, 30$. Right panel: Measured jet thickness along jet. The dotted lines indicate the location of re-collimation shock.
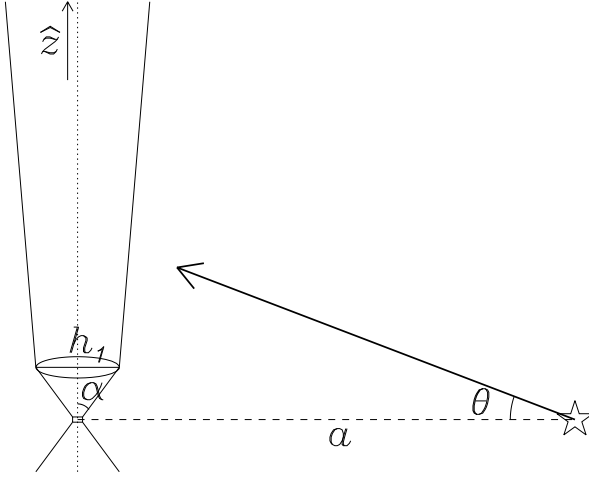
Figure 6. Schematic figure. α is a jet semi-opening angle, a is a separation, θ is an inclination angle from the orbital plane, and h_1 is the jet thickness at the collimation shock.
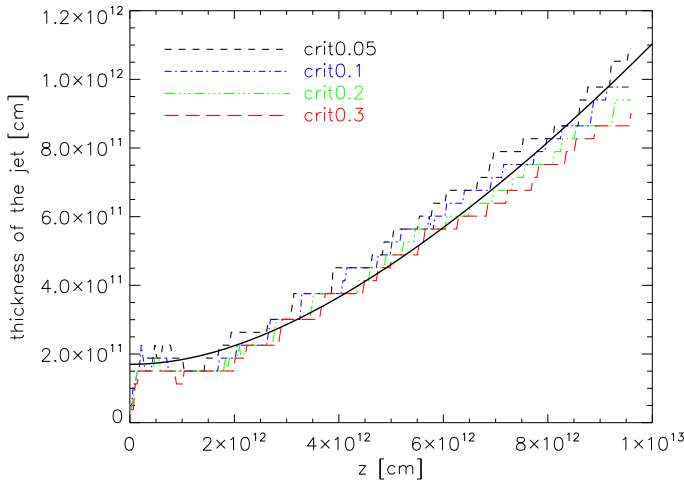
Figure 7. The thickness of the jet in SphWind_E37 model. The solid black line represents the analytic solution from eq. (12) with the parameters appropriate for the model of SphWind_E37, and dashed and dot-dashed lines indicate the numerical results for different choices of the threshold used to determine whether a computational cell belongs to the jet.

lated by the jet can be derived as a function of z:

$$
\begin{aligned}
\Delta\Phi_{m,\text{wind}} &= \int_0^{t(z)} dt \int_{-h/2}^{h/2} dy \int_{-X(y)/2}^{X(y)/2} dx \nabla_x P_{\text{bow}} \\
&= \int_0^z \frac{dz'}{v_{\text{jet}}} \int_{-h/2}^{h/2} dy P_{\text{bow}} \\
&= \int_0^z \frac{dz'}{v_{\text{jet}}} h(z') P_{\text{bow}} \\
&= \int_0^z \frac{dz'}{v_{\text{jet}}} \rho_{\text{wind},0} v_{\text{wind}}^2 h_1 \left(\frac{a^2}{a^2 + z'^2} \right)^{2-1/\gamma} \\
&= \frac{h_1 \rho_{\text{wind},0} v_{\text{wind}}^2}{v_{\text{jet}}} a f(z, \gamma) \\
&= \frac{h_1 \dot{M}_{\text{wind}} v_{\text{wind}}}{4\pi a \, v_{\text{jet}}} f(z, \gamma) \qquad (14)
\end{aligned}
$$

where

$$
f(z, \gamma) \equiv \int_0^{z/a} dy \left(\frac{1}{1 + y^2} \right)^{2-1/\gamma} \qquad (15)
$$

which can be expressed as a combination of hypergeometric functions, but is most easily evaluated numerically.

In the first order (small bending angle) approximation we are making here, the ratio of transverse to longitudinal momentum is equal to the bending angle (*i.e.*, the angle between the local and the initial velocity vector or tangent vector of the jet as a function of z):

$$
\begin{aligned}
\psi(z, \gamma) &= \frac{v_\perp}{v_\parallel} = \frac{\Delta\Phi_{m,\text{wind}}}{\Phi_{m,\text{jet}}} \\
&= \frac{\dot{M}_{\text{wind}} v_{\text{wind}} v_{\text{jet}} h_1}{4\pi a \, L_{\text{jet,kin}}} f(z, \gamma) \qquad (16)
\end{aligned}
$$

The asymptotic value for $z \longrightarrow \infty$ can then be evaluated in terms of elementary Gamma functions by taking the appropriate limit of $f(z, \gamma)$:

$$
\begin{aligned}
\psi_\infty &= \lim_{z \to \infty} \psi(z, \gamma) = \frac{\dot{M}_{\text{wind}} v_{\text{wind}} v_{\text{jet}} h_1}{4\pi a \, L_{\text{jet,kin}}} \lim_{z \to \infty} f(z, \gamma) \\
&= \frac{\dot{M}_{\text{wind}} v_{\text{wind}} v_{\text{jet}} h_1}{4\pi a \, L_{\text{jet,kin}}} \frac{\sqrt{\pi}}{2} \frac{\Gamma(3/2 - 1/\gamma)}{\Gamma(2 - 1/\gamma)} \qquad (17)
\end{aligned}
$$

where

$$f(\gamma) \equiv \lim_{z \to \infty} f(z, \gamma) = \frac{\sqrt{\pi}}{2} \frac{\Gamma(3/2 - 1/\gamma)}{\Gamma(2 - 1/\gamma)} \qquad (18)$$

with $f(4/3) = 1.2$ and $f(5/3) = 1.07$ for a relativistic and non-relativistic monatomic gas, respectively. Hence, for otherwise identical parameters, the jet should be bent about 10% less in the case of $\gamma = 5/3$ compared to the case of $\gamma = 4/3$, showing that the effect of adiabatic index on ψ_∞ is moderate. Figure 8 shows the dependence of the $f(\gamma)$ on the adiabatic index from $\gamma = 4/3$ to $\gamma = 5/3$.

While h_1 cannot be measured observationally, we can express eq. (17) in terms of the observable jet width on VLBA scales, $h_{\rm obs}$ measured at distance $z_{\rm obs} \gg a$, or alternatively, the observed opening angle $\alpha_{\rm obs} = h_{\rm obs}/(2z_{\rm obs})$:

$$\psi_\infty = \frac{h_{\rm obs}}{a} \left(\frac{a^2}{a^2 + z_{\rm obs}^2} \right)^{1/\gamma} \frac{\dot{\rm M}_{\rm wind} v_{\rm wind} v_{\rm jet}}{4\pi L_{\rm jet,kin}} f(\gamma)$$

$$\approx \alpha_{\rm obs} \left(\frac{z_{\rm obs}}{a} \right)^{1-2/\gamma} \frac{\dot{\rm M}_{\rm wind} v_{\rm wind} v_{\rm jet}}{2\pi L_{\rm jet,kin}} f(\gamma) \qquad (19)$$

where $z_{\rm obs} = z_{\rm VLBA}/\sin(\theta_{\rm LOS})$ and $\alpha_{\rm obs}$ are assumed to be corrected for foreshortening given the line-of-sight inclination angle $\theta_{\rm LOS}$ of the jet.

We carried out one test simulation, Sph-Wind_E37_gam166, with $\gamma = 5/3$ for the jet fluid, and the resulting jet appears more straight, consistent with analytic expression (see Figure 9). Note that the ratio is independent of the orbital separation, a, because of the relationship $h_1 = 2z_1 \sin\alpha_0$, where z_1 can be calculated from eq. (9).
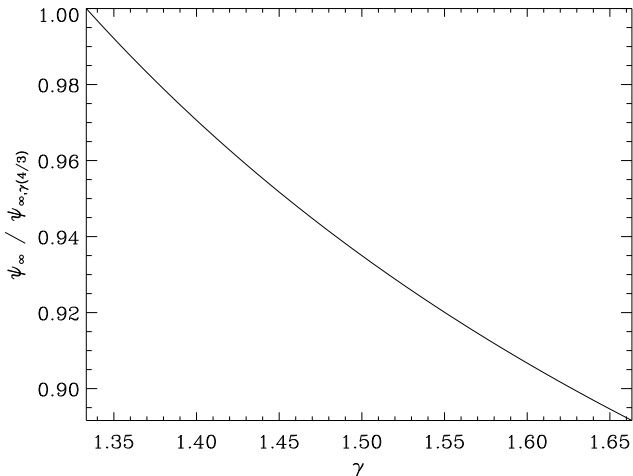
Figure 8. The asymptotic jet bending angle as a function of adiabatic index, γ. The angle is normalized by the one for the case of $\gamma = 4/3$.

While these expressions are strictly non-relativistic, it is straight forward to show that in the ultra-relativistic case, the estimate for the bending angle ψ is increased by a factor of $\sqrt{2}$ over the non-relativistic case (where the velocity is simply set to $v = c$). Thus, the lower limits we derive below on $L_{\rm jet}$ from observational upper limit on ψ becomes *stronger* in the relativistic case.

In the small bending angle regime, our analytic expressions are consistent with the simulation results, as shown in Figure 9. In the figure, the solid curves were constructed by integrating the jet trajectory along z, given the analytic expression for the transverse velocity $v_{\rm jet,\perp} \approx \psi v_{\rm jet}$ from eq. (16) in the small angle approximation [*i.e.*, $d(x - x_0)/dz = \tan\psi$ where x_0 is the location of the black hole]. For small bending angles, the figure shows excellent agreement between the model and the simulations.

As expected, for the case of stronger jet power, $L_{\rm jet} = 10^{37}\,{\rm ergs\,s^{-1}}$, the jet is only moderately bent from the initial direction, while lower power jets are more strongly affected by the winds, resulting in a higher degree of deflection. In the figure, the solid lines represent analytic trajectories calculated by eqs. (13)-(14) and dashed lines indicate the asymptotic direction estimated in eq. (17).

In the case of our fiducial simulation (jet power $L_{\rm jet} = 10^{36}\,{\rm ergs\,s^{-1}}$), the jet becomes dynamically unstable around $z = 2.5 \times 10^{12}\,{\rm cm}$, which leads to significant broadening of the jet and enhanced bending, and, as a result, the jet begins to deviate from the analytic estimate. Further quantitative analysis of the turbulent structures and their effect to the evolution of the jet is beyond this work. It is, however, clear from the simulations that jet-instability will only *increase* $\Delta\Phi_{m,\rm wind}/\Phi_{m,\rm jet}$ and ψ_∞.

Thus, our small jet bending angle approximation can be considered a robust lower limit of the actual jet bending angle. Figure 10 shows the fractional deviation of the numerical result from the analytic estimate as a function of jet bending angle. Our analytic formula is very accurate for bending angles smaller than $20°$. For larger bending angles, the approximation breaks down.

4.3. *The Effects of Orbital Motion and Wind Acceleration*

We carried out two simulations including the effects of orbital motion(SphWind_E36_rot) and radiatively driven winds (SphWind_E36_acc) in order to evaluate the importance of both effects by comparing to our standard model.

Figure 9 shows that, for small bending angles, the effects are small and the results with and without orbital motion and wind acceleration are consistent with each other. This is not surprising, since the centrifugal force from the orbital motion is about 3 orders of magnitude less than radiative force, and the Coriolis force acts purely in the transverse direction. Therefore, our setup with fixed black hole and star positions is sufficiently accurate in the context of this analysis.

We reach a similar conclusion about the effect of radiative acceleration. The model with a radiatively driven wind has a negligibly small difference in the momentum flux of the stellar wind at the binary separation compared to our standard model. It implies that our assumption that the wind reaches terminal velocity before encountering the jet is valid.

For large bending angles, where dynamical instabilities lead to rapid jet disruption and increased bending, the deviation between individual simulations is noticeable, as expected given the time variability of the jet trajectory on those scales.

4.4. *Jet Bending as a Diagnostic of Jet Power: The case of Cygnus X-1*

In the limit that $\Delta\Phi_{m,\text{wind}} > \Phi_{m,\text{jet}}$, bending in the simulation is so strong that the jet is dynamically disrupted, rather than simply bent. The interaction disperses the jet into a broad, no longer collimated flow at much lower velocity than the jet velocity. We would not expect such a strongly bent jet to survive as an observable radio jet. This suggests a simple diagnostic: If a stable compact jet is observed intact in an HMXB, one can conclude that the bending angle should be moderate.

For example, the compact VLBA jet of Cyg X-1 is extended, with a scale length z_{VLBA} of approximately 15 mas (compared to the angular scale of the orbital separation a of 0.1 mas), with an upper limit to the half-opening angle of $\alpha_{\text{VLBA}} < 2°$ where the viewing angle, θ_{LOS}, is approximated to $40°$ (Stirling et al. 2001). Combined with the other fiducial parameters of Cyg X-1, a robust limit can be derived from the observed stable compact jet by taking the bending angle to be $\psi_\infty = \Delta\Phi_{m,\text{wind}}/\Phi_{m,\text{jet}} \ll \pi/2$, which gives

$$\left(\frac{L_{\text{jet}}}{10^{37}\,\text{ergs s}^{-1}}\right)\left(\frac{\sin\theta_{\text{LOS}}}{\sin 40°}\right)^{-2/\gamma}\left(\frac{\alpha_{\text{VLBA}}}{2°}\right)^{-1}$$
$$\times\left[\frac{f(\gamma=4/3)}{f(\gamma)}\right]\left[\left(\frac{z_{\text{VLBA}}}{a}\right)/150\right]^{2/\gamma-1}\left[\frac{(150)^{2/\gamma-1}}{(150)^{1/2}}\right]$$
$$\times\left(\frac{v_{\text{wind}}}{1.6\times 10^8\,\text{cm s}^{-1}}\right)^{-1}\left(\frac{v_{\text{jet}}}{0.6\,c}\right)^{-1}$$
$$\times\left(\frac{\dot{M}_{\text{wind}}}{2.6\times 10^{-6}\,\text{M}_\odot\,\text{yr}^{-1}}\right)^{-1} \gg 8.5\times 10^{-3} \quad (20)$$

where $\gamma = 4/3$ in our standard model. For the case of $\gamma = 5/3$, the limit increases to 3.9×10^{-2} due to relatively shallow increase in jet thickness along the jet, which requires a larger initial opening angle α_0 and thus a wider initial jet to give the same observed $\alpha_{\text{VLBA}} \lesssim 2°$.

This limit can be made more specific by the fact that the jet appears to be oriented in the same direction in separate VLBA radio observations, taken during different orbital phases (Stirling et al. 2001). The data suggest a possible moderate bending on the jet of less then $10°$ on VLBA scales. Given the stability of the jet, we consider this an upper limit on the jet bending angle, *i.e.*, $\psi_\infty \lesssim 10°$, which translates to

$$L_{\text{jet}} \gtrsim 7.6\times 10^{35}\,\text{ergs s}^{-1}$$
$$\times\left(\frac{\dot{M}_{\text{wind}}}{2.6\times 10^{-6}\,\text{M}_\odot\,\text{yr}^{-1}}\right)\left(\frac{v_{\text{wind}}}{1.6\times 10^8\,\text{cm s}^{-1}}\right)$$
$$\left(\frac{v_{\text{jet}}}{0.6\,c}\right)\left(\frac{\alpha_{\text{VLBA}}}{2°}\right)\left(\frac{\sin\theta_{\text{LOS}}}{\sin 40°}\right)^{2/\gamma}\left[\frac{f(\gamma)}{f(\gamma=4/3)}\right]$$
$$\left[\left(\frac{z_{\text{VLBA}}}{a}\right)/150\right]^{1-2/\gamma}\left[\frac{(150)^{1-2/\gamma}}{(150)^{-1/2}}\right], \quad (21)$$

where for $\gamma = 5/3$, this limit increases to $3.5\times 10^{36}\,\text{ergs s}^{-1}$.

This lower limit on the jet power is consistent with the range of jet powers quoted in Gallo et al. (2005), Russell et al. (2007), and Sell et al. (2015), but derived from a completely independent, likely more robust argument.
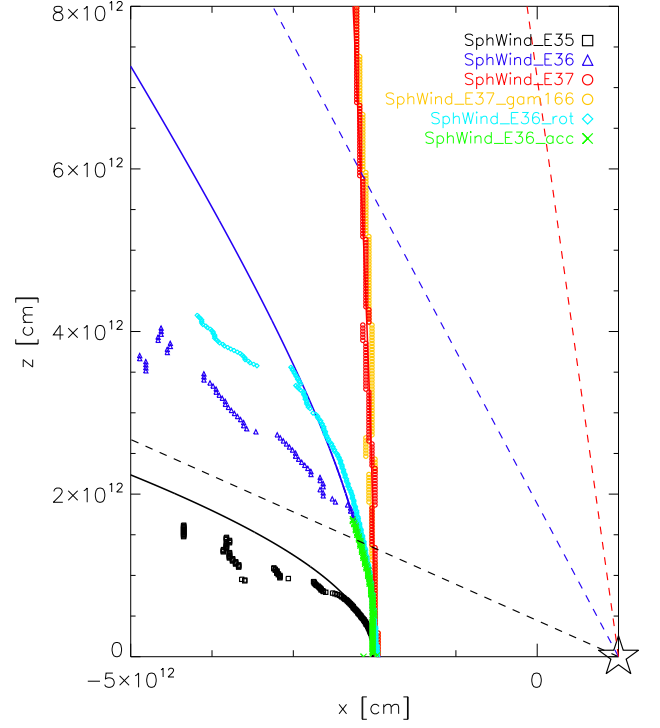
Figure 9. Comparison of numerical results with analytic estimates. Each symbol represents the numerical result, and solid lines indicate the analytic jet trajectories. Dashed lines indicate the asymptotic towards which the jet is expected to converge analytically.
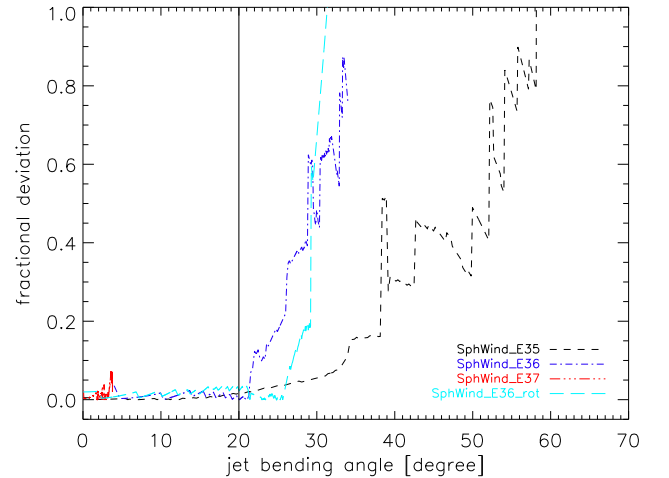
Figure 10. Fractional deviation of the jet trajectory between numerical result and analytic formula as a function of jet bending angle.

4.5. *Off-axis Jets*

When the progenitor of the compact object in an X-ray binary undergoes a supernova explosion in its last stage

of stellar evolution, it likely receives a substantial kick. Such a kick is capable of leaving the binary in an orbit where the spin and the orbital angular momentum are misaligned (Brandt & Podsiadlowski 1995).

The spin will slowly align with the orbital axis through a combination of the Lense-Thirring effect and the internal viscosity of the accretion disk (Bardeen & Petterson 1975). Martin et al. (2008) showed that the alignment time scale is a few times smaller than the life time of the mass-transfer state, typically $t_{align} \sim 10^6 - 10^8$ yr. While this implies that in most XRBs, spin and orbital angular momentum are likely aligned, it is plausible that they are mis-aligned in a sub-set of young XRBs, especially for HMXBs, given the short main sequence life time of the companion.

In this situation, the jet-wind interaction will become phase dependent. Because the jet propagation and bending time is short compared to the binary orbital period, the analysis presented above applies only to the phase of the binary orbit where the jet is perpendicular to the orbital separation vector $\vec{a}$. For any given orbit, there are two such node points. During other orbital phases, one side of the jet will approach the companion star (*i.e.*, the minimum distance between jet and star is smaller than the orbital separation), while the other side of the jet is receding; the approaching side will be more strongly bent.

We performed a set of simulations to explore this scenario. We define the inclination angle $\pi/2 - \theta_0$ between the initial direction of the jet $\hat{\vec{z}}$ and the orbital separation vector $\vec{a}$, such that

$$\theta_0 = \pi/2 - \cos^{-1}\left(\hat{\vec{z}} \cdot \hat{\vec{a}}\right) \qquad (22)$$

i.e., $\theta_0 = 0$ implies the jet is perpendicular to $\vec{a}$, corresponding to the case discussed so far, while $\theta_0 = \pi/2$ implies a jet maximally inclined, pointed at the star/away from it. In other words, in the limit of instantaneous reaction of the jet to orbital changes, the angle $\phi_{\mathrm{jet,orbit}}$ between the jet and the orbital velocity vector does not affect jet bending (reflected also in the fact that most of our simulations neglect orbital motion entirely). Clearly, for any non-zero jet inclination relative to the orbital axis, the angle θ_0 will change as a function of orbital phase.

Because jet bending reacts instantaneously to orbital changes, the jet will always propagate in a plane spawned by the initial jet direction and the orbital separation vector, to order considered here. For circular binary orbits, the asymptotic bending angle therefore only depends on θ_0, and only implicitly depends on binary phase through θ_0.

We now extend our analytic formula to the off-axis case. The momentum flux of the jet will be the same, but the accumulated momentum flux of the stellar wind changes with inclination angle. The accumulated wind momentum per unit jet length is then (following eq. (14)):

$$\Delta\Phi_{m,\mathrm{wind}}(\theta) = \frac{h_1 \dot{\mathrm{M}}_{\mathrm{wind}} v_{\mathrm{wind}}}{4\pi\, a\, v_{\mathrm{jet}}}\, \tilde{f}(z,\gamma,\theta_0), \qquad (23)$$

where

$$\tilde{f}(z,\gamma,\theta_0) \equiv (\cos\theta_0)^{-2+1/\gamma} \int_{-\tan\theta_0}^{z/a} dy \left(\frac{1}{1+y^2}\right)^{2-1/\gamma}. \qquad (24)$$

We can use the ratio of the accumulated wind momentum to jet momentum per unit length, eq. (17), to derive the asymptotic bending angle ψ_∞

$$\psi_\infty = \frac{\dot{\mathrm{M}}_{\mathrm{wind}} v_{\mathrm{wind}} v_{\mathrm{jet}}\, h_1}{4\pi\, a\, L_{\mathrm{jet,kin}}}\, \tilde{f}(\gamma,\theta_0), \qquad (25)$$

where

$$\tilde{f}(\gamma,\theta_0) \equiv \lim_{z\to\infty} \tilde{f}(z,\gamma,\theta_0). \qquad (26)$$

It is obvious that if θ_0 is 0, this expression reduces to eq. (17).

For the approaching side of the jet, which is inclined towards the companion star in our simulation (Figure 11), $\tilde{f}(\gamma,\theta_0)$ is monotonically increasing, resulting in stronger bending of the jet.

If θ_0 is larger than some value, the jet collides with the star. Given the binary parameters for Cygnus X-1, this limit angle is 62.18°. The impact region where the jet directly encounters the star is marked by the grey area in the Figure 11&12.

Figure 12 shows ψ_∞ as a function of θ_0, assuming h_1 is kept constant in the approaching side of the jet where it heads toward the companion star. From this analysis we can infer the jet bending angle for an initially off-axis jet. As one might expect, a more inclined jet will be more strongly bent. The right panel of Figure 12 shows ψ_∞ with respect to the orbital plane. The figure shows a monotonic increase of jet bending angle with initial jet inclination.

Figure 13 shows the momentum ratio and asymptotic angle for the receding jet. For jets with higher inclination angles, the bending angle is reduced.
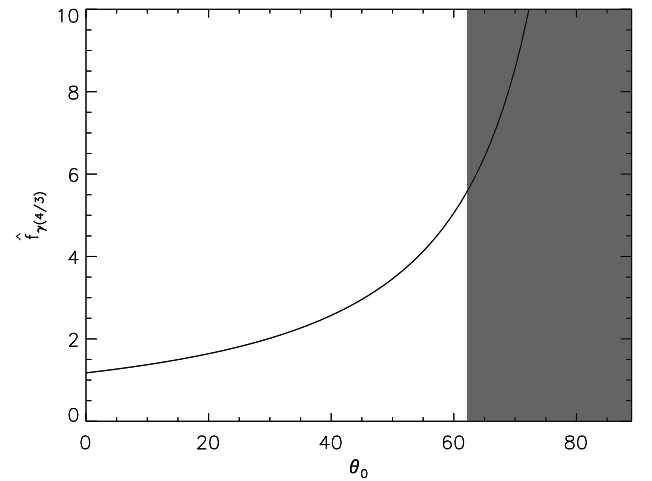

Figure 11. Variation of $\tilde{f}$ as a function of θ_0. The grey area shows the impact region where the approaching jet runs into the stellar surface.

Figure 14 shows density maps for several cases of the misaligned simulations. All other parameters are the
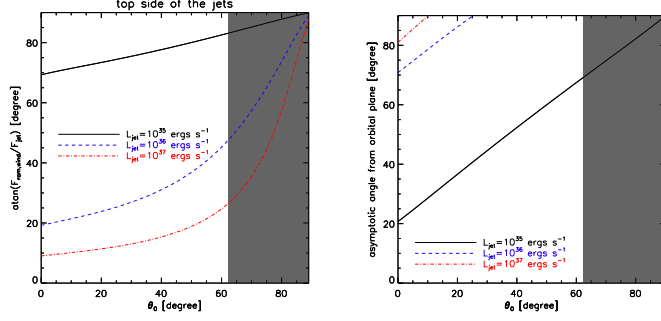
Figure 12. Case of approaching jet, initially pointing towards the companion star. Left panel: The ratio of the accumulated wind momentum flux to the jet momentum flux as a function of θ_0. Right panel: Asymptotic jet bending angle with respect to the orbital plane. The grey area shows the impact region where the approaching jet runs into the stellar surface.
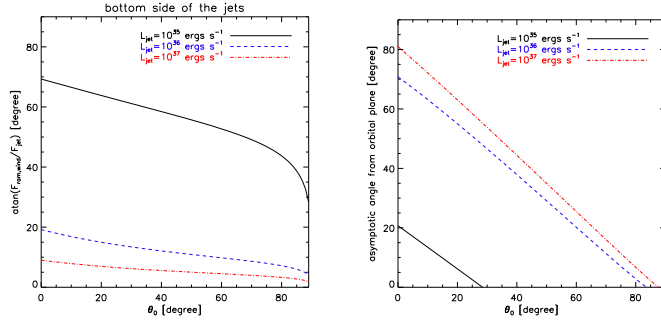
Figure 13. Case of receding jet, initially pointing away from the companion star. Same panels as in Figure 12

same as in our standard model, SphWind_E36. The inclination angles are 30°, 60°, 75°, respectively. The magenta solid line represents the analytic jet trajectory which is derived using the assumption of pressure balance between the jet and the ambient medium. For all cases, the approaching jet shows some degree of disruption and dynamical instability and the analytic approximation breaks down for bending angles larger than about 20°. On the other hand, the figures show that our analytic approach is acceptable for the receding side of the jets.

As one would expect from simple geometric considerations, while a jet launched perpendicular to the orbital separation $\vec{a}$ is bent symmetrically on either side, an inclined jet shows asymmetric behavior between approaching jet and receding jet. Such a configuration would lead to increased jet bending in the approaching jet. Our limit on the jet power in Cyg X-1 was derived under the most conservative assumption that the jet is not inclined relative to the orbital axis. Because jet bending and disruption increase for inclined jets, the possible inclination of the jet will strengthen our limit on the jet power.

Szostek & Zdziarski (2007) argued that in Cygnus X-1, the orbital modulation of radio emission occurs due to free-free absorption in the asymmetric wind as a function of orbital phase, and the observed phase lag of the modulation with respect to the orbital phase could be attributed to the time delay for the emission from the dy-

namically curved jet. However, the jet bending we studied in this work is likely not the cause of the phase lag, because the bending direction is parallel to the orbital separation vector, leading to only very small phase lags due to light-travel-time delays, while the observed phase lags would require bending in the direction against the orbital velocity, as argued by Szostek & Zdziarski (2007).

For higher jet inclination angles, (*e.g.* SphWind_E36_60deg or SphWind_E36_75deg), both jet and counter-jet will impact the star once per orbit, leading to jet disruption and reformation; one might thus expect to observe episodic jet eruption from such a system.

4.6. *The case of Cygnus X-3*

We can apply a similar argument to the case of Cygnus X-3, an HMXB consisting of a compact object and a Wolf-Rayet companion. In this case, it is still not clear whether the compact object is a black hole or a neutron star, but the observational evidence of collimated jet-like structures is strong in multi-epoch radio maps (Martí et al. 2001). The radio jets with γ-ray flares occur during bright soft X-ray states or during state transitions (Szostek et al. 2008; Tavani et al. 2009).

Dubus et al. (2010) suggested that the jet of Cygnus X-3 is inclined relative to the orbital plane ($20° < \psi_{\rm jet} < 80°$) in order to obtain good fits to the gamma-ray modulation, with a significant offset between the jet footpoint and the site of the gamma-ray emission.

This estimate does not take potential jet bending into account. In fact, as shown above, even if the orbital angular momentum and the jet axis are aligned, we should expect some bending to occur, and the asymptotic jet direction will change over the course of the binary orbit. As a result, the precession of the jet occurs on a time scale, $\tau_{\rm precess} \approx \tau_{\rm orbit}$ in our model. We should point out that there is currently no evidence for (or against) jet precession in Cygnus X-3. The observed gamma-ray modulation can be explained by an inclined jet. An inclined jet is likely bent more than a jet perpendicular to the orbital plane, so jet bending by the jet-wind interaction may have to be taken into account in detailed models of Cygnus X-3.

Assuming the initial jet direction is perpendicular to the orbital plane, we can estimate the bending angle from eq. (17) from the binary and jet parameters $L_{\rm jet} = 10^{38}\,{\rm ergs\,s^{-1}}$, $\dot{M}_{\rm wind} = 10^{-5}\,{\rm M_\odot\,yr^{-1}}$, $a = 3 \times 10^{11}{\rm cm}$, $v_{\rm wind} = 10^8\,{\rm cm\,s^{-1}}$, and $v_{\rm jet} = 0.5\,c$ as used by Dubus et al. (2010).

Note that Cygnus X-3 is a considerably tighter system with higher inferred jet energy than Cygnus X-1, while the momentum flux from its neighboring Wolf-Rayet star is higher than that from OB companion in Cygnus X-1. In terms of the fiducial parameters given above, the jet bending angle can be calculated from eqs. (9) and (17)
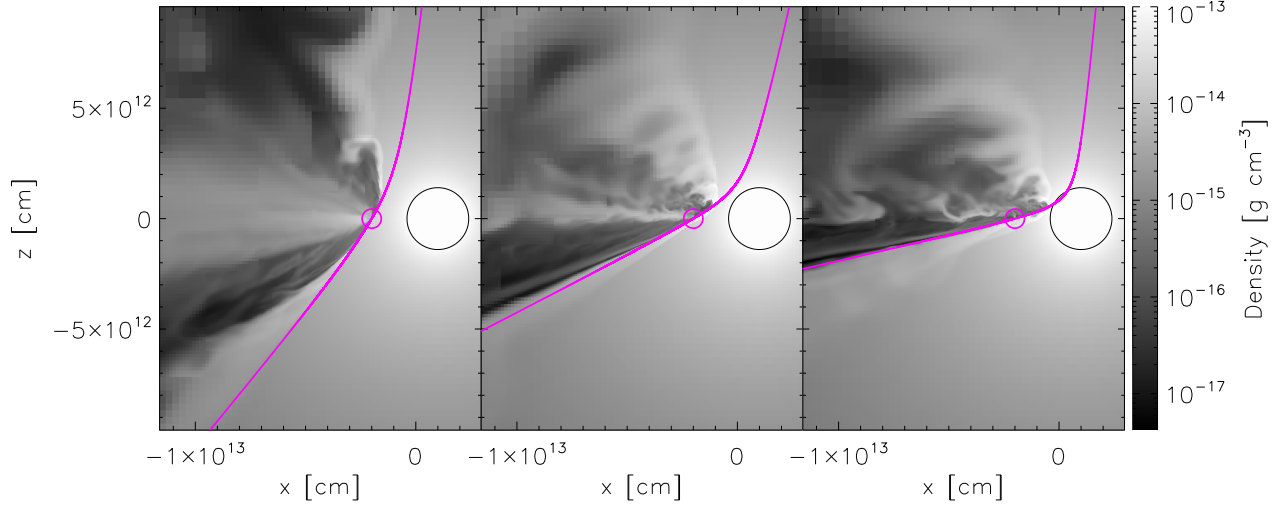
Figure 14. Density maps for off-axis jets, deviating from perpendicular direction to orbital plane: 30°, 60°, 75° from left to right panel. The solid magenta line indicates the analytical trajectory of the jet. The magenta circle indicate the location of the black hole.

as

$$\psi_\infty \sim 2.35°$$

$$\times \left(\frac{\dot{M}_{wind}}{10^{-5}\,M_\odot\,yr^{-1}}\right)^{1/2} \left(\frac{v_{wind}}{10^8\,cm\,s^{-1}}\right)^{1/2} \left(\frac{v_{jet}}{0.5\,c}\right)^{1/2}$$

$$\left(\frac{L_{jet}}{10^{38}\,ergs\,s^{-1}}\right)^{-1/2} \left[\frac{f(\gamma)}{f(\gamma = 4/3)}\right] \left[\frac{\sin\alpha_0}{\sin(2°)}\right], \tag{27}$$

indicating that for jet bending to be important, the initial opening angle of the jet would have to be significantly larger than a few degrees, or the jet would have to be strongly misaligned with the orbital axis, with the jets very closely approaching the stellar surface for part of the orbit.

4.7. *Caveats*

Our simulations were carried out using an isotropic and homogeneous stellar wind model. This assumption allows us to study the dynamics of jet-wind interaction in a simple analytic framework. Several complications will affect this process in ways not included in this paper.

4.7.1. *X-ray Ionization*

Firstly, the X-ray flux from the accretion disk may be intense enough to ionize the circum-stellar gas, so the wind can be reduced or quenched, decreasing the jet bending angle. Line driving is likely inefficient in the illuminated portion of the wind if the ionization parameter is above a critical threshold. Conversely, the X-ray illumination can itself produce thermal wind driving by heat input. The exact configuration of the wind is therefore not entirely clear.

However, from the fact that the black hole in Cygnus X-1 is accreting from the companion wind, the illuminated portion of the wind must be of similar density to that assumed in the shadowed region, which suggests that the estimates presented above will not be changed drastically by the effects of ionization of the wind.

4.7.2. *Clumping*

More importantly, the stellar wind from OB-type stars is likely clumpy (Oskinova et al. 2012). Poutanen et al. (2008) suggested that the wind in Cygnus X-1 is clumped, based on dips in the X-ray lightcurve.

This situation was simulated by P12. Because global simulations that incorporate clumped winds with realistic clump sizes and densities will be computationally impossible in the foreseeable future, given the large dynamic range and resolution required to capture the mass in small clumps, our paper should be considered complementary to the work presented in P12.

While a detailed treatment of clumping in our simulations is beyond the scope of this paper, we will briefly discuss how significant clumping would affect the results of our simulations. For a fixed mass loss rate and wind velocity, the net effect of wind clumping will depend on the filling factor, the average size of the clumps, and the density contrast. Since secular bending is facilitated by the pressure gradient across the jet, we should expect bending in the presence of clumps to be reduced by the amount the momentum flux in the hot low-density background component of the wind is reduced relative to an un-clumped wind. The reduction is set by the density ratio of the hot/low density background component ρ_{hot} to the density ρ_{wind} of an un-clumped wind of the same emission measure.

Since ρ_{hot} is poorly constrained, we cannot easily quantify the reduction expected in the bending angle by the presence of clumps. Clearly, if ρ_{hot} is of the same order as the estimates of ρ_{wind} used above, our results will be unaffected. However, if $\rho_{hot} \ll \rho_{wind}$, the amount of secular bending of the jet will be reduced by the density ratio ρ_{hot}/ρ_{wind}.

In the case of O-star winds in HMXBs, the presence of clumps in the illuminated side of the wind is even less well constrained, given the effects X-ray ionization may have on clump formation.

For all these reasons, a general statement about how our results change in the presence of clumping is difficult to make. However, considering the possible limits of clump sizes and density, we can estimate under which circumstances the jet would be able to propagate through the wind without disruption and derive similar

constraints on the jet power for a given set of clump parameters.

If the density contrast between the clumps and the background wind is small, corrections should naturally be minor and the limit on the jet power from eq. (21) will hold. If the density contrast is large and most of the mass is carried in clumps, the effect will depend on the average size of the clumps, relative to the width h of the jet:

Large clumps: If the clumps are large compared to the cross section of the jet, jet-clump interaction will be disruptive, and the conclusions of P12 hold, *i.e.*, the jet will be disrupted unless it is sufficiently powerful to escape, in the case investigated by P12, $L_{\rm jet} \gtrsim 10^{37} \, {\rm ergs \, s^{-1}}$, similar to the conclusion we reach in this paper, with the main difference being that interaction with a clumpy wind introduces significant stochasticity. It has been suggested by Zdziarski et al. (2011) that fluctuations in the radio light curve may be an expression of such interaction.

Small clumps: If the clumps are much smaller than the cross section of the jet, such that the typical clump radius satisfies $R_{\rm clump} \ll h_{\rm jet}$, they will act like bullets passing through the jet, generating small bow shocks that slow down a small fraction of the jet. Small clumps will only globally disrupt the jet if **(a)** the covering fraction $f_{\rm clumps}$ of clumps is larger than unity *and* **(b)** the total mass within clumps is sufficiently high to stop the jet fluid. *Both* conditions must be met for the jet to be disrupted by a wind whose mass flux is dominated by small clumps.

Note that in this case, jet disruption will not be stochastic, since it requires the presence of many small clouds passing through the jet continuously, rather than a few large clouds. Since the jet in Cygnus X-1 is *not* disrupted continuously, at least one of the two conditions for jet disruption must be violated. We can now estimate the constraints the observed stability of the jet against wind disruption place on the jet and cloud parameters.

(a) Low covering fraction: The covering fraction $f_{\rm cover}$ of clumps is given by

$$f_{\rm cover} = \int_0^\infty dz \frac{f}{R_{\rm clump}} \sim \frac{a f_{\rm vol}}{R_{\rm clump}} \qquad (28)$$

where z is the path length along the jet, a is the orbital separation, and $f_{\rm vol}$ is the clump volume filling factor. If $f_{\rm cover} \gg 1$, the jet *may* be disrupted if the total mass within clumps is sufficiently high to stop the jet fluid ($f_{\rm clumps} \gg 1$ is a necessary condition for jet disruption). Conversely, a *sufficient but not necessary* condition for the jet *not* to be disrupted is that the covering fraction of clumps is small, $f_{\rm cover} \ll 1$, or

$$f_{\rm vol} \ll \frac{R_{\rm clump}}{a} \ll 1 \qquad (29)$$

The condition that the emission measure of the clumped wind is the same as that of the un-clumped wind (in the optically thin limit) gives a clump volume filling fraction of $f_{\rm vol} = \rho_{\rm wind}^2/\rho_{\rm clump}^2$ or $\sqrt{f_{\rm vol}} \, \rho_{\rm clump}/\rho_{\rm wind} = 1$. With eq. (29), the condition on $f_{\rm cover}$ implies that the wind mass loss rate

must satisfy

$$\dot{\rm M}_{\rm wind,clumped} = \frac{\rho_{\rm clump} f_{\rm vol}}{\rho_{\rm wind}} \dot{\rm M}_{\rm wind} = \sqrt{f_{\rm vol}} \, \dot{\rm M}_{\rm wind}$$

$$\ll \dot{\rm M}_{\rm wind} \sqrt{\frac{R_{\rm clump}}{a}} \ll \dot{\rm M}_{\rm wind} \qquad (30)$$

(b) Low mass density: A second necessary condition for clumps in the wind to significantly disrupt the jet is that the clump mass $\Delta {\rm M}_{\rm clump}$ intercepted by the jet exceed the inertial mass of the jet plasma, ${\rm M}_{\rm jet}$. Conversely, a second *sufficient but not necessary* condition for the jet *not* to be disrupted is

$${\rm M}_{\rm jet} = \int_0^\infty dz A_{\rm jet} \rho_{\rm jet,inertial}$$

$$\gg \int_0^\infty dz A_{\rm jet} f \rho_{\rm clump} = \Delta {\rm M}_{\rm clump} \qquad (31)$$

which we can simplify as the condition

$$\rho_{\rm jet} \gg f_{\rm vol} \rho_{\rm clump} \qquad (32)$$

Assuming that the location of the re-collimation shock of the jet is set by the ram pressure of the hot, low density background gas of the clumped wind, we can use eqs. (5) and (8) to write this condition as

$$f_{\rm vol} \frac{\rho_{\rm clump}}{\rho_{\rm hot}} \ll \frac{v_{\rm wind}^2 \mathcal{M}_{\rm jet,0}^2}{v_{\rm jet}^2} = \frac{v_{\rm wind}^2}{c_{\rm s,jet,0}^2} \qquad (33)$$

where $\rho_{\rm hot} \ll \rho_{\rm wind} \ll \rho_{\rm clump}$ is the density of the hot background wind in the clumped wind scenario. This condition can be written as a limit on the wind mass flux:

$$\dot{\rm M}_{\rm wind,clumped} \ll \frac{\rho_{\rm hot}}{\rho_{\rm wind}} \frac{v_{\rm wind}^2}{c_{\rm s,jet,0}^2} \dot{\rm M}_{\rm wind} \ll \dot{\rm M}_{\rm wind} \qquad (34)$$

where the last inequality reasonably assumes that $c_{\rm s,jet,0} > v_{\rm wind}$.

In summary, we can distinguish the following three cases, one of which must apply to Cygnus X-1:

1. The wind is not strongly clumped (that is, the mass flux in the diffuse/background wind is comparable to the mass flux used in this paper, even if clumps are present). In this case, our limit in eq. (21) applies and the jet must be powerful to propagate through the wind.

2. The wind is strongly clumped, with large clumps of size $R \gtrsim h$; in this case, the analysis of P12 applies and the jet must be powerful to propagate through the wind.

3. The wind is strongly clumped, with small clumps of size $R \ll h$; in this case, the mass loss rate must be orders of magnitude below the mass loss rate of an un-clumped wind, given the observed emission measure and lack of jet disruption. In this case, we cannot use the observed lack of jet disruption/bending to derive a limit on the jet power.

Thus, (a) either the wind mass loss rate must be orders of magnitude smaller than the nominal wind parameters for a uniform wind for the companion star, with important implications for wind formation in HMXBs, and/or (b) the jet power must be large [eq. (21)], similar to the conclusion reached from energy estimates of the large scale nebula.

5. CONCLUSION

We performed global hydrodynamic simulations to study jet-wind interaction in the wind of the companion star in HMXBs. The interaction results in the jet being bent with a characteristic bending angle that depends on the properties of the jet and the wind. Using the small bending angle approximation, we derived a simple analytic formula for the asymptotic bending angle. The formula is consistent with the numerical results, and it can be used to analyze observations of jets in HMXBs. We showed that the analysis is valid for bending angles smaller than about $20°$.

We applied the formula to two observed HMXBs, Cygnus X-1 and Cygnus X-3. We constrained the jet power in Cygnus X-1 to be $L_{\rm jet} \gtrsim 10^{36}\,{\rm ergs\,s^{-1}}$ from the lack of observed precession of the VLBA jet. This limit is consistent with previous estimates, but derived from completely independent arguments and likely more robust.

Given Cygnus X-3 parameters, we argued that the jet bending is likely not significant, unless the jet in Cygnus X-3 has a large opening angle α or is significantly less powerful than estimated in previous studies.

The main caveat in the application of this model to observed HMXBs is the lack of knowledge about the properties of wind clumping in massive stars. We discussed conditions under which clumping will affect the analysis of jet bending presented in this paper, and under which clumps themselves will lead to observable dynamic disruption of the jet. We showed that, if wind clumping is dynamically important for the jet-wind interaction in Cygnus X-1, our limit on the jet power holds unless the wind mass loss rate is orders magnitude below the nominal wind parameters derived for a uniform wind (in which case we would not be able to constrain the jet power from the lack of disruption or bending by the wind).

REFERENCES

Bardeen, J. M., & Petterson, J. A. 1975, ApJ, 195, L65
Begelman, M. C., Rees, M. J., & Blandford, R. D. 1979, Nature, 279, 770
Brandt, N., & Podsiadlowski, P. 1995, MNRAS, 274, 461
Brocksopp, C., Tarasov, A. E., Lyuty, V. M., & Roche, P. 1999, A&A, 343, 861
Castor, J. I., Abbott, D. C., & Klein, R. I. 1975, ApJ, 195, 157
Castor, J. L. 1974, MNRAS, 169, 279
Dubus, G., Cerutti, B., & Henri, G. 2010, MNRAS, 404, L55
Freeland, E., & Wilcots, E. 2011, ApJ, 738, 145
Friend, D. B., & Castor, J. I. 1982, ApJ, 261, 293
Fryxell, B., Olson, K., Ricker, P., et al. 2000, ApJS, 131, 273
Gallo, E., Fender, R., Kaiser, C., et al. 2005, Nature, 436, 819
Gies, D. R., & Bolton, C. T. 1982, ApJ, 260, 240
Gies, D. R., Bolton, C. T., Blake, R. M., et al. 2008, ApJ, 678, 1237
Hadrava, P., & Čechura, J. 2012, A&A, 542, A42
Heinz, S., & Begelman, M. C. 2000, ApJ, 535, 104
Heinz, S., Brüggen, M., Young, A., & Levesque, E. 2006, MNRAS, 373, L65
Heinz, S., Grimm, H. J., Sunyaev, R. A., & Fender, R. P. 2008, ApJ, 686, 1145
Hjellming, R. M., Stewart, R. T., White, G. L., et al. 1990, ApJ, 365, 681
Lee, D., & Deane, A. E. 2009, Journal of Computational Physics, 228, 952
Martí, J., Paredes, J. M., & Peracaula, M. 2001, A&A, 375, 476
Martin, R. G., Reis, R. C., & Pringle, J. E. 2008, MNRAS, 391, L15
McNamara, B. R., & Nulsen, P. E. J. 2007, ARA&A, 45, 117
Miller, J. M., Wojdowski, P., Schulz, N. S., et al. 2005, ApJ, 620, 398
Mirabel, I. F., & Rodríguez, L. F. 1999, ARA&A, 37, 409
Morsony, B. J., Miller, J. J., Heinz, S., et al. 2013, MNRAS, 431, 781
Orosz, J. A., McClintock, J. E., Aufdenberg, J. P., et al. 2011, ApJ, 742, 84
Oskinova, L. M., Feldmeier, A., & Kretschmar, P. 2012, MNRAS, 421, 2820
Owocki, S. P., Castor, J. I., & Rybicki, G. B. 1988, ApJ, 335, 914
Perucho, M., & Bosch-Ramon, V. 2012, A&A, 539, A57
Pooley, G. G., Fender, R. P., & Brocksopp, C. 1999, MNRAS, 302, L1
Poutanen, J., Zdziarski, A. A., & Ibragimov, A. 2008, MNRAS, 389, 1427
Puls, J., Vink, J. S., & Najarro, F. 2008, A&A Rev., 16, 209
Russell, D. M., Fender, R. P., Gallo, E., & Kaiser, C. R. 2007, MNRAS, 376, 1341
Sell, P. H., Heinz, S., Richards, E., et al. 2015, MNRAS, 446, 3579
Stirling, A. M., Spencer, R. E., de la Force, C. J., et al. 2001, MNRAS, 327, 1273
Szostek, A., & Zdziarski, A. A. 2007, MNRAS, 375, 793
Szostek, A., Zdziarski, A. A., & McCollough, M. L. 2008, MNRAS, 388, 1001
Tavani, M., Bulgarelli, A., Piano, G., et al. 2009, Nature, 462, 620
van Kerkwijk, M. H. 1993, A&A, 276, L9
Wiersema, K., Russell, D. M., Degenaar, N., et al. 2009, MNRAS, 397, L6
Yoon, D., Morsony, B., Heinz, S., et al. 2011, ApJ, 742, 25
Zdziarski, A. A., Mikołajewska, J., & Belczyński, K. 2013, MNRAS, 429, L104
Zdziarski, A. A., Skinner, G. K., Pooley, G. G., & Lubiński, P. 2011, MNRAS, 416, 1324